Acta Mech 224, 2311–2329 (2013)
DOI 10.1007/s00707-013-0933-z

Cristian Marchioli · Alfredo Soldati

Rotation statistics of fibers in wall shear turbulence

Received: 26 November 2012 / Revised: 20 May 2013 / Published online: 3 August 2013

Abstract In this paper, the rotation of rigid fibers is investigated for the reference case of turbulent channel flow. The aim of the study is to examine the effect of local shear and turbulence anisotropy on the rotational dynamics of fibers with different elongation and inertia. To this aim, statistics of the fiber angular velocity, Ω, are extracted from direct numerical simulation of turbulence at shear Reynolds number $Re_\tau = 150$ coupled with Lagrangian tracking of prolate ellipsoidal fibers with Stokes number, St, ranging from 3 to 100 and aspect ratio, λ, ranging from 1 to 50. Accordingly, the fiber-to-fluid density ratio ranges from $S \simeq 7$ (for $St = 1$, $\lambda = 50$) to $S \simeq 3{,}470$ (for $St = 100$, $\lambda = 1$). Statistics are compared one to one with those obtained for spherical particles to highlight effects due to elongation. Results for mean and fluctuating angular velocities show that elongation is important for fibers with small inertia ($St \leq 5$ in the present flow-fiber combination). For fibers with larger inertia, elongation has an impact on fiber rotation only in the streamwise and wall-normal directions, where mean values of Ω are zero. It is also shown that, in the center of the channel, the Lagrangian autocorrelation coefficients of Ω and corresponding rotational turbulent diffusivities match the exponential behavior predicted by the theory of homogeneous dispersion. In this region of the channel, the probability density function of fiber angular velocities is generally close to Gaussian, indicating that particle rotation away from solid walls can be modeled as a diffusion process of the Ornstein–Uhlenbeck type at stationary state. In the strong shear region (comprised within a distance of 50 viscous units from the wall in the present simulations), fiber anisotropy adds to flow anisotropy to induce strong deviations on fiber rotational dynamics with respect to spherical particles. The database produced in this study is available to all interested users at https://www.fp1005.cism.it.

1 Introduction

The dynamics of rigid fibers in turbulent shear flow plays a crucial role in many industrial applications such as pulp and paper production [1], polymer processing [2], and molding of fiber-reinforced composites [3], to name a few. In all these processes, quality and material properties of the final product are significantly affected by the spatial and orientational distribution of fibers, which is in turn dominated by local velocity gradients [4], fluid shear, and flow inhomogeneities [5], hence the need for a thorough understanding of how fibers are dispersed and oriented by turbulence [6].

C. Marchioli (✉) · A. Soldati
Department of Fluid Mechanics, CISM, Piazza Garibaldi 18, 33100 Udine, Italy
E-mail: marchioli@uniud.it
Tel.: +39-0432-558006
Fax: +39-0432-558027

A. Soldati
E-mail: soldati@uniud.it

In addition to specific industrial applications, fiber dynamics is of fundamental interest since statistical characterization of fiber translation and rotation is crucial for the validation of rheological models. A critical step in developing such models is the dependency of the extra non-Newtonian stress, produced by the addition of fibers to the Newtonian carrier fluid, on fiber orientation distribution [7]. This dependency is usually described via a probability density function of fiber orientation, which requires closure of its higher-order moments and knowledge of translational and rotational dispersion coefficients [7,8]. Limiting our discussion to rotation, accurate statistics of angular velocity at varying fiber inertia and elongation are deemed foundational to quantify rotational dispersion [4], which is known to depend on the ratio of fiber length to Lagrangian integral length scale of the flow [8].

A possible approach for modeling rotation of fibers in turbulence is to describe the time-dependent evolution of fiber angular velocity as a stochastic (random walk) process in orientation space [9]: In analogy with the translational motion of tracers and inertial particles in homogeneous isotropic turbulence (HIT), one can hypothesize that the Lagrangian time series of angular velocity are characterized by a Gaussian probability distribution with Markovian properties (meaning that the distribution at the current state is determined only by the distribution at the previous state). Based on this hypothesis, fiber rotation can be described within the theory of diffusion as a Ornstein–Uhlenbeck (OU) process [10]. The OU process is completely characterized by a statistically stationary Gaussian distribution and autocovariance, which takes the specific form of a negative exponential: using a general notation, $R(\tau) = \alpha^2 \exp(-\tau/T_*)$, with α^2 the variance of the Gaussian distribution and T_* the integral timescale of the process [11].

This modeling approach assumes that both translational diffusion and rotational diffusion are homogeneous and isotropic [12]. Many numerical and experimental studies have been performed [13–18], which demonstrate that this assumption is acceptable for unbounded flows where dispersion is indeed stationary and Gaussian (see [19] and references therein for more details). Other investigations [20–22] have shown that the laws governing homogeneous dispersion may be partly extended to wall-bounded shear flows (specifically, turbulent channel flow), demonstrating in particular that Lagrangian velocity autocorrelations can be approximated with a decaying exponential if particles are not sampling near-wall regions of high turbulence anisotropy. All these studies, however, are concerned with spherical particles and focus on particle translational motion. Much less effort has been devoted to exploring the applicability of standard diffusion laws to rotational motion of particles with non-spherical shape, as in the case of fibers. To our knowledge, previous modeling attempts focus on HIT [6,8,9] and thus neglect effects due to turbulence anisotropy. Recent numerical and experimental studies [4,6], however, show that orientation of elongated fibers is correlated with local velocity gradients and that the strength of this correlation is strongly influenced by the fiber shape. These findings suggest that anisotropy of fibers adds to anisotropy of turbulence to deviate fiber behavior (in particular, rotation rates) from that predicted by stationary Gaussian dispersion models: The Gaussian process, which is valid for spherical point parcels in HIT, may thus fail when the particles and/or the turbulence become anisotropic. They also raise issues about the adequacy of the simulation approaches currently used to obtain large statistical samples [4,23]. Most of these are in fact based on Lagrangian tracking of fibers leaving their anisotropic behavior to Jeffery orbits [24]. Such approaches, based on representing fibers as pointwise, have obvious advantages and some limitations. Advantages are associated with the simplicity of the pointwise assumption (availability of force models, no need for complicated interpolation schemes, easy coding). Limitations are associated with the non-local nature of fiber motion (especially when the fiber is larger than the small scales of the flow), which may prevent Lagrangian tracking from capturing the complexity added by the fiber elongation.

In this work, our main objective is to examine the effect of local shear and flow anisotropy on the rotational dynamics of fibers with different elongation and inertia. This analysis is exploited to verify capability and limitations of the Lagrangian point-fiber approach and to assess the extent to which diffusion laws can be applied to describe fiber rotational dispersion in wall-bounded turbulence. More specifically, we are interested in assessing the possibility of modeling rotation as an OU process depending both on flow parameters (shear, anisotropy) and on fiber parameters (inertia, elongation). To perform our study, we analyze the Lagrangian autocorrelation curves of the fiber angular velocity and the corresponding rotational turbulent diffusivity, which provides a simple measure of the characteristic time required for a complete rotation cycle of the fiber. We also examine the probability density function (PDF) of angular velocity components to verify whether these exhibit Gaussian properties, typical of diffusive processes, within the flow. In doing so, we hypothesize that similar calculations performed for the Lagrangian fluid vorticity (the vorticity measured along the trajectory of fluid tracers) would reveal a qualitatively similar behavior. To our knowledge, the statistics discussed in the present work are not available in the archival literature: they are proposed here to provide a public DNS-based repository of accurate post-processed data that can be used for benchmarking and model validation.

2 Problem statement

2.1 Physical problem and methodology

The database from which rotation statistics were extracted is the same as that described in [25]. Reference flow configuration and numerical methodology are also the same: these are recalled in the following to make the paper self-contained.

The reference flow configuration chosen to simulate wall shear turbulence is Poiseuille flow of incompressible, isothermal, and Newtonian fluid in a plane channel at friction Reynolds number $Re_\tau = u_\tau h/\nu = 150$, where u_τ is the friction velocity based on the mean wall shear stress and on fluid density, ν is fluid viscosity, and h is the channel half-height. The corresponding bulk Reynolds number is $Re = u_b h/\nu = 2{,}250$, where $u_b = 1.77$ m/s is the bulk velocity. The Reynolds number based on the hydraulic diameter is $Re_D \simeq 9{,}000$. We performed direct numerical simulation (DNS) using the pseudo-spectral flow solver described in [26], imposing periodic boundary conditions in the streamwise (x) and spanwise (y) directions and no-slip conditions at the walls. Time integration of fluid uses a second-order Adams–Bashforth scheme for the nonlinear terms (which are calculated in a pseudo-spectral way with de-aliasing in the periodic directions) and an implicit Crank–Nicolson scheme for the viscous terms. The non-dimensional step size for time integration is 0.03 in wall units. The size of the computational domain is $1{,}885 \times 942 \times 300$ wall units (i.e., in terms of variables identified with the superscript "+" made dimensionless using ν and u_τ) in x, y and z, discretized with $128 \times 128 \times 129$ grid nodes.

Lagrangian fiber dynamics is treated in the same way as in [23,27,28]. The translational equation of motion of an individual fiber is given by the linear momentum equation $\mathrm{d}\mathbf{u}_p/\mathrm{d}t = \mathbf{F}/m$, where $\mathbf{u}_p$ is the fiber velocity, $\mathbf{F}$ is the total hydrodynamic drag force acting on the fiber, and $m = \frac{4}{3}\pi a^3 \lambda \rho_p$ is the fiber mass. Here, a is the the semiminor axis, $\lambda = b/a$ is the aspect ratio of the ellipsoid with semimajor axis b, and ρ_p is the density of the particle. The expression for $\mathbf{F}$ used in our simulations was first derived by [29] for an ellipsoid under creeping flow conditions: $\mathbf{F} = \mu \mathbf{K}(\mathbf{u}_{@p} - \mathbf{u}_p)$, where μ is the fluid dynamic viscosity, $\mathbf{K}$ is the resistance tensor, and $\mathbf{u}_{@p}$ is the fluid velocity at fiber position. The resistance tensor $\mathbf{K}$ is expressed with respect to the Eulerian (inertial) frame of reference, $\mathbf{x} = <x, y, z>$. Two other Cartesian coordinate systems are used to describe fiber motion (see Fig. 1): a Lagrangian fiber frame of reference, $\mathbf{x}' = <x', y', z'>$, attached to the fiber with origin at the fiber center of mass; and a co-moving frame of reference, $\mathbf{x}'' = <x'', y'', z''>$, attached to the fiber with origin at the fiber center of mass and axes parallel to the inertial frame. Given these frames, the resistance tensor is computed as $\mathbf{K} = \mathbf{A}^t \mathbf{K}' \mathbf{A}$, where $\mathbf{K}'$ is the resistance tensor computed in the fiber frame, $\mathbf{A}$ is the orthogonal transformation matrix comprising the direction cosines (which, in turn, are defined by the Euler parameters), and $\mathbf{A}^t$ is its transpose. The rotational motion of the fiber is governed by the equation: $\mathrm{d}(\mathbf{I} \cdot \Omega')/\mathrm{d}t + \Omega' \times (\mathbf{I} \cdot \Omega') = \mathbf{N}'$, where $\mathbf{I}$ is the moment of inertia tensor, Ω' is the angular velocity of the fiber, and $\mathbf{N}'$ the torque acting on the fiber, all computed in the fiber frame.

The complete set of equations considered to describe translational and rotational motion of the fibers, written in dimensionless form, reads as:

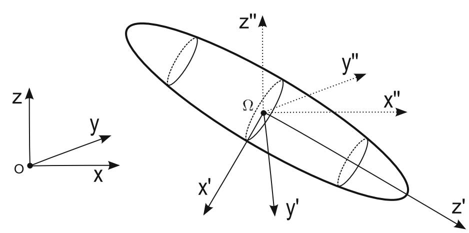

Fig. 1 Sketch of the ellipsoidal fiber and Cartesian coordinate systems: inertial frame $\mathbf{x}$, particle frame $\mathbf{x}'$, and co-moving frame $\mathbf{x}''$

$$\text{Kinematics}\begin{cases}\dfrac{\mathrm{d}\mathbf{x}_{p,(G)}}{\mathrm{d}t}=\mathbf{u}_p\\[2mm]\dfrac{\mathrm{d}e_0}{\mathrm{d}t}=\dfrac{1}{2}\left(-e_1\Omega_{x'}-e_2\Omega_{y'}-e_3\Omega_{z'}\right)\\[2mm]\dfrac{\mathrm{d}e_1}{\mathrm{d}t}=\dfrac{1}{2}\left(e_0\Omega_{x'}-e_3\Omega_{y'}+e_2\Omega_{z'}\right)\\[2mm]\dfrac{\mathrm{d}e_2}{\mathrm{d}t}=\dfrac{1}{2}\left(e_3\Omega_{x'}+e_0\Omega_{y'}-e_1\Omega_{z'}\right)\\[2mm]\dfrac{\mathrm{d}e_3}{\mathrm{d}t}=\dfrac{1}{2}\left(-e_2\Omega_{x'}+e_1\Omega_{y'}+e_0\Omega_{z'}\right)\end{cases}\tag{1}$$

$$\text{Dynamics}\begin{cases}\dfrac{\mathrm{d}\mathbf{u}_p}{\mathrm{d}t}=\dfrac{3}{4\lambda Sa^2}\mathbf{K}\cdot(\mathbf{u}_{@p}-\mathbf{u}_p)\\[2mm]\dfrac{\mathrm{d}\Omega_{x'}}{\mathrm{d}t}=\Omega_{y'}\Omega_{z'}\left(1-\dfrac{2}{1+\lambda^2}\right)+\dfrac{20\left[(1-\lambda^2)f'+(1+\lambda^2)(\xi'-\Omega_{x'})\right]}{(\beta_0+\lambda^2\gamma_0)(1+\lambda^2)Sa^2}\\[2mm]\dfrac{\mathrm{d}\Omega_{y'}}{\mathrm{d}t}=\Omega_{x'}\Omega_{z'}\left(\dfrac{2}{1+\lambda^2}-1\right)+\dfrac{20\left[(\lambda^2-1)g'+(\lambda^2+1)(\eta'-\Omega_{y'})\right]}{(\alpha_0+\lambda^2\gamma_0)(1+\lambda^2)Sa^2}\\[2mm]\dfrac{\mathrm{d}\Omega_{z'}}{\mathrm{d}t}=\dfrac{20}{(\alpha_0+\beta_0)Sa^2}(\chi'-\Omega_{z'})\end{cases}\tag{2}$$

with $\mathbf{x}_p$ the fiber location vector, e_i the Euler parameters, Ω_i the fiber angular velocity components, and S the fiber-to-fluid density ratio. Quantities f' and g' are the elements of the fluid rate of the strain tensor $S_{ij}=\frac{1}{2}(u_{i,j}+u_{j,i})$ while ξ', η', and χ' are the elements of the fluid rate of rotation tensor $\omega_{ij}=\frac{1}{2}(u_{i,j}-u_{j,i})$:

$$f'=\frac{1}{2}\left(u_{z',y'}+u_{y',z'}\right),\; g'=\frac{1}{2}\left(u_{x',z'}+u_{z',x'}\right),\tag{3}$$

$$\xi'=\frac{1}{2}\left(u_{z',y'}-u_{y',z'}\right),\; \eta'=\frac{1}{2}\left(u_{x',z'}-u_{z',x'}\right),\; \chi'=\frac{1}{2}\left(u_{x',y'}-u_{y',x'}\right).\tag{4}$$

The parameters α_0, β_0, and γ_0 are given as [24]:

$$\begin{aligned}\alpha_0=\beta_0&=\frac{2\lambda^2\sqrt{\lambda^2-1}+\lambda\cdot\ln\left(\frac{\lambda-\sqrt{\lambda^2-1}}{\lambda+\sqrt{\lambda^2-1}}\right)}{2(\lambda^2-1)^{3/2}},\\ \gamma_0&=-\frac{2\sqrt{\lambda^2-1}+\lambda\cdot\ln\left(\frac{\lambda-\sqrt{\lambda^2-1}}{\lambda+\sqrt{\lambda^2-1}}\right)}{(\lambda^2-1)^{3/2}}.\end{aligned}\tag{5}$$

Equation (1) are integrated in time using a standard fourth-order Runge–Kutta scheme, while Eq. (2) are solved using a mixed explicit/implicit differencing procedure developed by [30]. The same timestep size as that of the fluid is used, and the total tracking time in wall units is $t^+=tu_\tau^2/\nu$=3,500. The relevant parameters for time integration are a, λ and the fiber response time [31]:

$$\tau_p=\frac{2a^2S}{9\nu}\frac{\lambda\ln(\lambda+\sqrt{\lambda^2-1})}{\sqrt{\lambda^2-1}}.\tag{6}$$

In this study, we have selected the following dimensionless values: $a^+=0.36$, $\lambda=1$ (spherical particles), 3, 10, 50, and $St=\tau_p^+=1, 5, 30, 100$. For this choice of values, the fiber-specific density is varied in the range $7<S<3{,}472$ [25]. To ensure converged statistics, swarms of $N=200{,}000$ fibers are tracked for each particle category, assuming dilute flow conditions (fiber volume fraction is always well below unity) and one-way coupling between the phases.

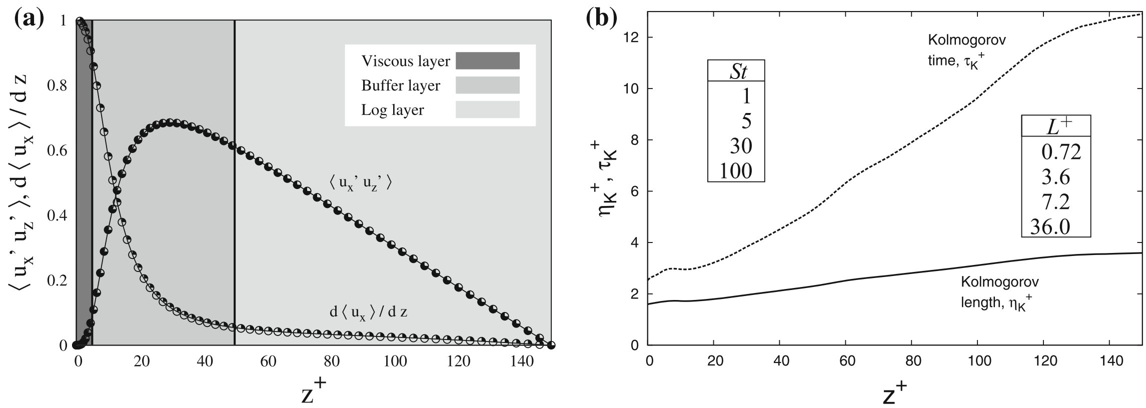

Fig. 2 **a** Shear stress components (viscous: $\mathrm{d}\langle u_x\rangle/\mathrm{d}z \propto \tau_{\mathrm{visc}}$; turbulent: $\langle u'_x u'_z\rangle \propto \tau_{\mathrm{turb}}$): colored areas represent the different subregions of the channel considered for computation of Lagrangian statistics. **b** Non-dimensional Kolmogorov length and timescales as a function of wall distance in the channel. Values of the Stokes number, St, and of the non-dimensional fiber length, L^+, are also shown in the inset tables to allow direct comparison with values of τ_K^+ and η_K^+, respectively

2.2 Simulation procedure

To compute rotation statistics, and in particular Lagrangian statistics (angular velocity autocorrelation coefficients and rotational diffusivities), we considered three distinct subregions of the channel, shown in Fig. 2a: viscous sublayer (comprised in the range $0 < z^+ < 5$ with z^+ the distance from the wall, dark-gray area in Fig. 2a), buffer layer ($5 < z^+ < 50$, intermediate gray area in Fig. 2a), and log layer ($50 < z^+ < Re_\tau$, light-gray area in Fig. 2a). These subregions are characterized by significantly different values of the shear stress components, as shown in Fig. 2a, and of the dissipative scales of the flow, shown in Fig. 2b, and may thus produce different fiber rotational dynamics. In particular, considering the indications of [4,6], we should expect changes in the distribution of angular velocities and rotation rates of the largest and more inertial fibers considered in the present study, which have non-dimensional length $L^+ = 2a^+\lambda$ (reported in the inset table of Fig. 2b) equal to several Kolmogorov length scales η_K^+ ($L^+/\eta_K^+ \sim \mathcal{O}(10)$ for the $\lambda = 50$ fibers). Statistics were first computed along the trajectory of each fiber and then the ensemble averaged over a time window $\Delta t^+ = 1{,}200$ based on the specific subregion within which the fiber was initially located.

3 Results

3.1 Angular velocity statistics

The non-dimensional ensemble-averaged angular velocity of the fibers is shown in Fig. 3 at varying fiber inertia. Only the spanwise component $\langle \Omega_y\rangle$ is shown since $\langle \Omega_x\rangle$ and $\langle \Omega_z\rangle$ are zero at all distances from the wall. Profiles in each panel highlight the effect of fiber elongation on $\langle \Omega_y\rangle$ for a specific value of St. Results for tracer particles, characterized by $St = 0$, are also shown (thick solid line). It can be observed that, regardless of inertia and shape, values of $\langle \Omega_y\rangle$ are much higher near the wall, where accumulation of the dispersed phase is known to occur [23,25], than outside of the buffer layer ($z^+ > 50$ in the present flow configuration), where elongation does not seem to alter the expectation value of fiber rotational dynamics significantly. Elongation is important in determining the near-wall behavior of $\langle \Omega_y\rangle$, which decreases as the fiber length increases. This implies that fibers spin slower than spherical particles, a consequence of fiber alignment in the longitudinal $x-z$ plane [23,25]. We also note that shape effects are evident for all values of the aspect ratio λ at small Stokes numbers ($St = 1,\ 5$), whereas longer fibers ($\lambda \geq 10$ in the present case) are required to induce significant reduction of $\langle \Omega_y\rangle$ at large Stokes numbers ($St = 30,\ 100$). Present results agree very well with those presented in [23] for $St = 5,\ 30$ and $\lambda = 1,\ 3,\ 10$ at slightly higher Re_τ.

In Figs. 4, 5, and 6, we show the root mean square (RMS) components of the angular velocity, $\langle \mathrm{RMS}(\Omega_i)\rangle$. As for the mean angular velocity, shape effects due to elongation are noticeable only inside the buffer layer. In agreement with [23], we find that these effects produce an increase of fluctuating angular velocity in the

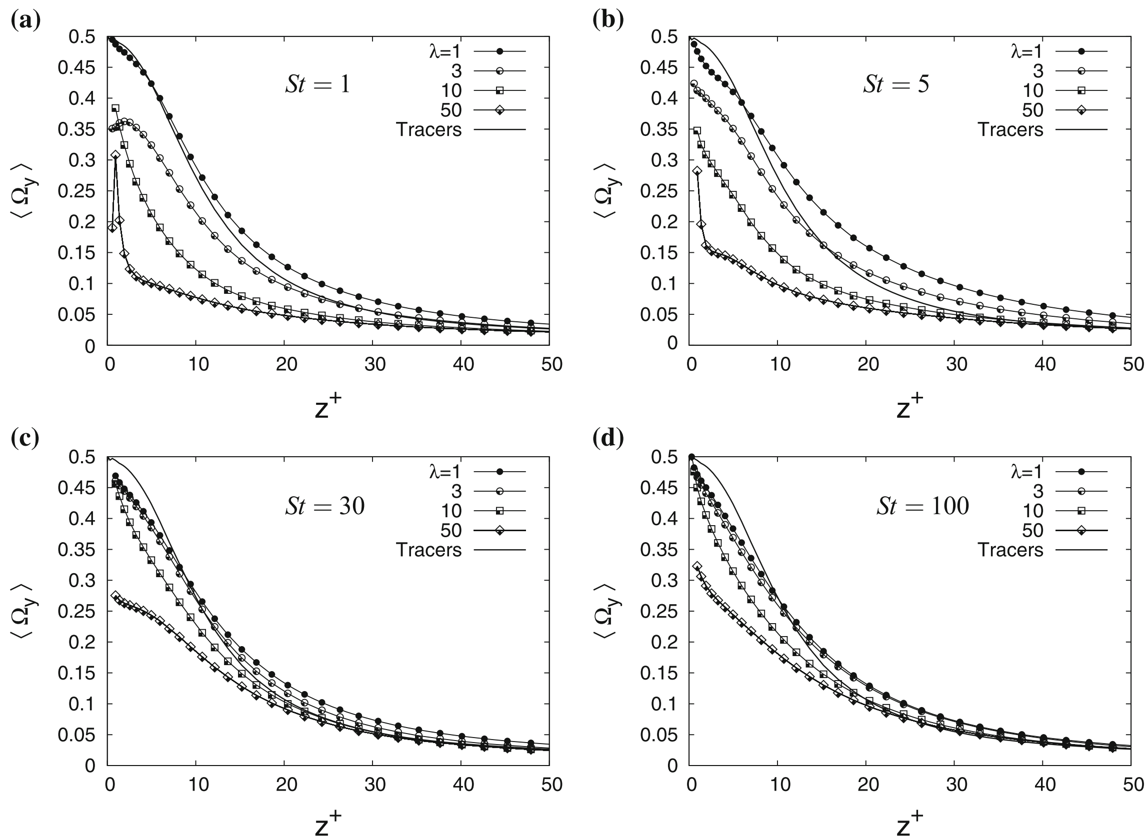

Fig. 3 Fiber spanwise angular velocity, $\langle \Omega_y \rangle$, inside the buffer layer ($z^+ < 50$). Profiles in each panel highlight the effect of fiber elongation (λ) on $\langle \Omega_y \rangle$: no significant λ-effect is observed outside the buffer layer

streamwise direction with λ regardless of fiber inertia (Fig. 4). We also observe that, for a fixed value of λ, an increase in fiber inertia (an increase of St) is associated with a decrease in $\langle \mathrm{RMS}(\Omega_x) \rangle$. These two findings indicate that elongation enhances fiber spin in the mean flow direction, whereas inertia damps it. Besides quantitative changes, elongation and inertia also produce significant modification of the near-wall shape of the streamwise RMS fiber rotation profiles, altering the position at which $\langle \mathrm{RMS}(\Omega_x) \rangle$ reaches the maximum value.

The effects just described are not as clear and less marked for the spanwise component, $\langle \mathrm{RMS}(\Omega_y) \rangle$. In particular, there is no monotonic increase in $\langle \mathrm{RMS}(\Omega_y) \rangle$ with λ and little or no modifications due to elongation are observed at large Stokes numbers ($St = 30,\ 100$ in Fig. 5c, d). The latter observation is in agreement with the results of [23] and can be explained considering again that larger-inertia fibers exhibit a higher tendency to align in the $x - z$ plane. In addition, the rotational inertia of these fibers is sufficiently high to damp spin intensities regardless of elongation. For small Stokes numbers ($St = 1,\ 5$, Fig. 5a, b), shape effects amplify modifications of fiber rotational behavior induced by the underlying turbulence.

The wall-normal RMS, $\langle \mathrm{RMS}(\Omega_z) \rangle$ (Fig. 6), exhibits a complex dependency on fiber inertia and elongation. Different from $\langle \mathrm{RMS}(\Omega_x) \rangle$, $\langle \mathrm{RMS}(\Omega_z) \rangle$ increases with λ only for the largest Stokes number ($St = 100$, Fig. 6d) and in the near-wall region: compared to spherical particles, fiber spin in the wall-normal direction is systematically reduced outside the viscous sublayer, this trend being more evident for the small Stokes number fibers ($St = 1,\ 5$, Fig. 6a, b, respectively). This is in agreement with our previous findings that fiber preferential alignment within the flow is unstable, particularly for higher inertia of the fiber and especially in the wall-normal direction. Fiber inertia and elongation destabilize in a non-trivial fashion alignment near the wall, which can be maintained for rather short times before fibers are set into rotation in the vertical plane [25].

3.2 Correlation statistics of the rotational motion

In this subsection, we characterize the rotational motion of the fibers by analyzing the autocorrelation coefficients of fiber angular velocity. We focus on the dynamics of fibers that have already interacted with turbulence

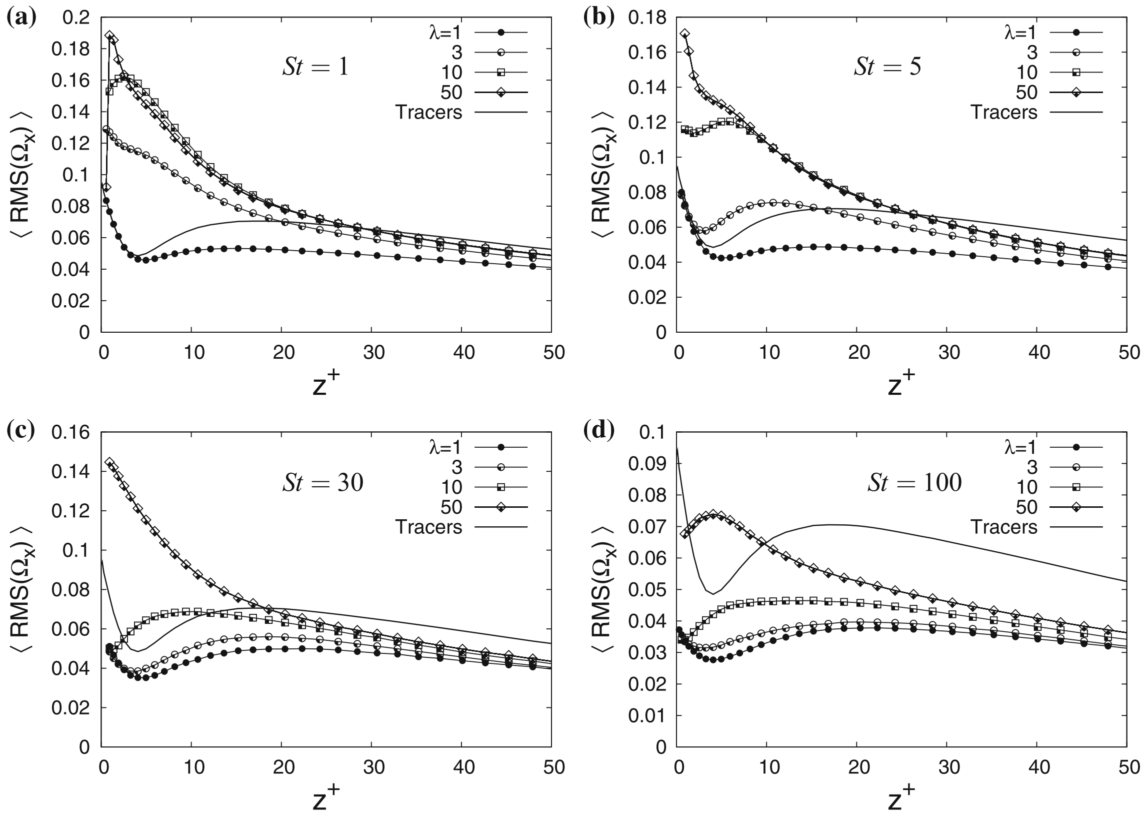

Fig. 4 Root mean square (RMS) of fiber streamwise angular velocity, $\langle \mathrm{RMS}(\Omega_x) \rangle$, inside the buffer layer ($z^+ < 50$). Profiles in each panel highlight the effect of fiber elongation (λ) on $\langle \mathrm{RMS}(\Omega_x) \rangle$: no significant λ-effect is observed outside the buffer layer

for a time period long enough to ensure that fiber alignment is correlated with the flow and has reached a statistical steady state. The angular velocity autocorrelation coefficients were computed for each subregion of the channel (viscous sublayer, buffer layer, and log layer) as:

$$R_{\Omega_i,\Omega_i}(\tau) = \frac{\left\langle \Omega_i' \left(\mathbf{x}_p(t_0), t_0\right) \Omega_i' \left(\mathbf{x}_p(t_0+\tau), t_0+\tau\right)\right\rangle}{\left\langle \Omega_i' \left(\mathbf{x}_p(t_0), t_0\right)^2\right\rangle^{1/2} \left\langle \Omega_i' \left(\mathbf{x}_p(t_0+\tau), t_0+\tau\right)^2\right\rangle^{1/2}}, \tag{7}$$

where $\langle\cdot\rangle$ represents an ensemble average over all fibers initially located in the subregion, and Ω_i' indicates the ith component of fiber fluctuating angular velocity. Note that $R_{\Omega_i,\Omega_i}(\tau)$ is computed along the Lagrangian trajectory $\mathbf{x}_p$ of the fiber and that the angular velocity that is being self-correlated is defined in the inertial frame of reference (x, y, z), not in the fiber frame of reference (x', y', z'). Since fibers were tracked in a statistically stationary flow, autocorrelations are independent of the initial time t_0. Statistical convergence of the numerical results was obtained by ensemble averaging over at least 10^4 trajectories.

Our aim is to verify whether and under which conditions (degree of shear and turbulence anisotropy, fiber inertia, and elongation) the Lagrangian autocorrelation can be approximated as a decaying exponential:

$$R_{\Omega_i,\Omega_i}(\tau) = e^{-\frac{\tau}{T_L^{ii}}}, \tag{8}$$

where T_L^{ii} is the Lagrangian integral timescale of the fiber angular velocity, defined as:

$$T_L^{ii} = \int_0^\infty R_{\Omega_i,\Omega_i}(\tau)\mathrm{d}\tau. \tag{9}$$

This quantity provides the simplest measure of the time span over which fiber orientation is self-correlated.

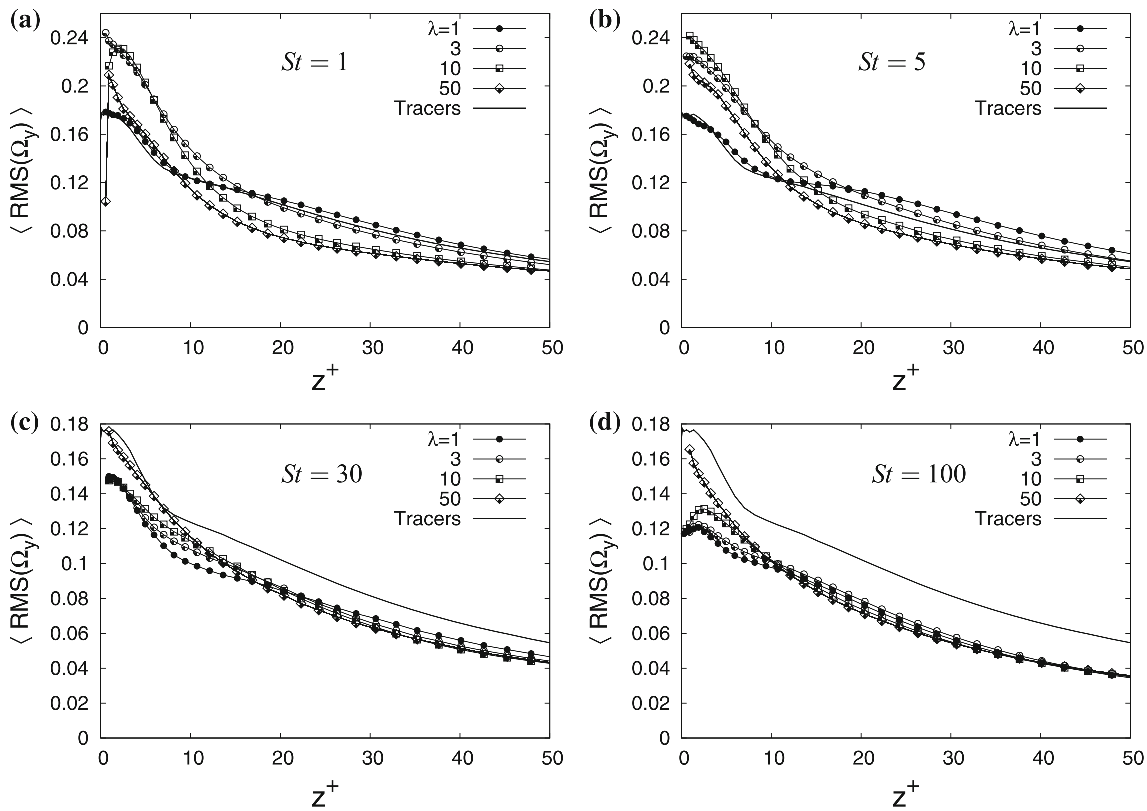

Fig. 5 Root mean square (RMS) of fiber spanwise angular velocity, $\langle \mathrm{RMS}(\Omega_y)\rangle$, inside the buffer layer ($z^+ < 50$). Profiles in each panel highlight the effect of fiber elongation (λ) on $\langle \mathrm{RMS}(\Omega_y)\rangle$: no significant λ-effect is observed outside the buffer layer

The Lagrangian autocorrelation coefficients R_{Ω_i,Ω_i} obtained for the different subregions of the channel at varying fiber inertia and elongation are shown in Figs. 7, 8, and 9. For the sake of brevity, results are shown only for the reference case of $St = 30$ fibers (resp. $\lambda = 10$ fibers) to highlight the effect of fiber elongation (resp. fiber inertia) on R_{Ω_i,Ω_i}. In the log layer (Fig. 7), where fibers are subject to weak mean shear and turbulence is nearly homogeneous and isotropic, all R_{Ω_i,Ω_i} curves show a neat exponential decay in time. It can be easily demonstrated that Eq. (8) provides a very good curve fitting (not shown here for clarity of visualization, evidence is provided in Sect. 3.3). This finding indicates that, if angular velocities have a Gaussian distribution, fiber rotation can be modeled as an OU process away from the channel walls. Profiles in Fig. 7 exhibit also similar persistence in time and drop to zero in a relatively short time span. Different behavior of the correlation coefficients was observed by [22] when examining the translational velocity of spherical particles dispersed in channel flow: in that case, coefficients show a stronger persistence in the streamwise direction than in either the spanwise or wall-normal directions. Left-hand panels in Fig. 7 demonstrate that shape effects on all R_{Ω_i,Ω_i} components are minor: this weak dependency can be attributed to the dominance of the large-scale flow structures on fiber rotation in the central portion of the channel. We remind that in this region the maximum fiber length ($L^+ = 36$, corresponding to $\lambda = 50$) is about 10 times the Kolmogorov length scale η_K^+. There is experimental evidence [4] that the rotational dynamics of rod-like particles in HIT should not exhibit appreciable change for a fiber length up to about $7\eta_K^+$. Based on this evidence, we expect all fiber families to align preferentially along the fluid velocity gradients depending only on inertia, not on elongation. Right-hand panels in the same figure indicate a more significant (and non-trivial) effect of fiber inertia on the decay rate of the coefficients. In all directions, the decay rate of R_{Ω_i,Ω_i} reaches a maximum for $St = 30$ and falls off at either side of this value. As a consequence of this behavior, Lagrangian timescales will change accordingly.

Results obtained for fibers initially located in the buffer layer (Fig. 8) show similar trends as in the log layer for the streamwise component R_{Ω_x,Ω_x} (panels a, b). The only noticeable change is a higher decay rate due to increased turbulent fluctuations that decorrelate rotation faster: this behavior indicates that flow

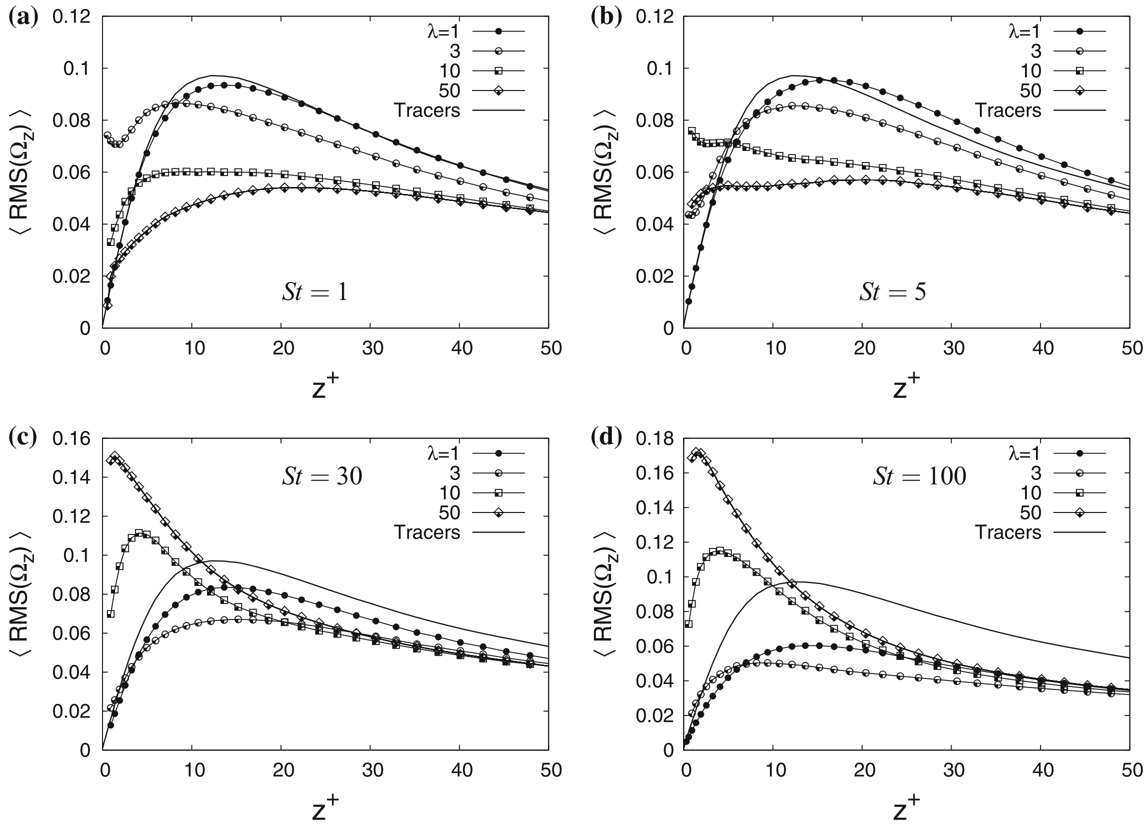

Fig. 6 Root mean square (RMS) of fiber wall-normal angular velocity, $\langle \mathrm{RMS}(\Omega_z)\rangle$, inside the buffer layer ($z^+ < 50$). Profiles in each panel highlight the effect of fiber elongation (λ) on $\langle \mathrm{RMS}(\Omega_z)\rangle$: no significant λ-effect is observed outside the buffer layer

structures with characteristic length and timescales smaller than those in the log layer do affect fiber motions in this "intermediate" region. Strong differences in the autocorrelation curves arise in the spanwise direction (panels c, d) and in the wall-normal direction (panels e, f). First, we now notice an effect of elongation: the autocorrelation coefficients decay slower for longer fibers, especially along the direction normal to the wall ($\lambda \geq 10$ in our flow-fiber combination). This is in agreement with the findings of [6], suggesting a decrease in rotation-rate variance with increasing fiber length. The point-fiber approach appears capable of reproducing (at least qualitatively) the combined effect of fiber anisotropy and turbulence anisotropy when fibers become sufficiently longer than the local dissipative scales of the flow to induce changes in the rotation rate (in the buffer layer, $L^+/\eta_K^+ \simeq 20$ for the $\lambda = 50$ fibers). Second, we observe that inertial effects are more evident: fibers with large inertia ($St \geq 30$) are characterized by rotational dynamics that are strongly persistent and self-correlated in time. As shown in Fig. 8f, the R_{Ω_z,Ω_z} curves for fibers with $St = 30$ and $St = 100$ do not reach zero values after 1,200 dimensionless time units.

Moving closer to the wall (viscous sublayer, Fig. 9), the behavior of the autocorrelation coefficients becomes more complex and resembles not at all that observed for fiber orientation and rotation rates in HIT [6]. The exponential decay is lost in most of the cases (as will be demonstrated in Sect. 3.3) and some curves exhibit negatively correlated parts that correspond to a change of sign in angular velocity with respect to the initial condition (see, e.g., Fig. 9b). It can also be observed that rotation of long fibers with high inertia ($\lambda \geq 10$, $St \geq 30$ in our simulations) in the wall-normal direction remains self-correlated over a time span much larger than that considered here for computing R_{Ω_z,Ω_z}.

The values of T_L^{ii} that could be extracted from numerical integration of Eq. (9) using the DNS+LPT data repository are summarized in Table 1 for all fiber sets investigated. From this table, the effect of fiber elongation on Lagrangian timescales can be deduced (i) in the log layer, where T_L^{ii} decreases as λ increases for the majority of cases, especially those with lower fiber inertia; and (ii) in the buffer layer, where T_L^{ii} is higher for spherical particles, reaches a minimum values for the $\lambda = 3$ fibers, and increases again for $\lambda = 10,\ 50$. In the viscous sublayer, rotational dynamics are more complex due to near-wall turbulence characteristics.

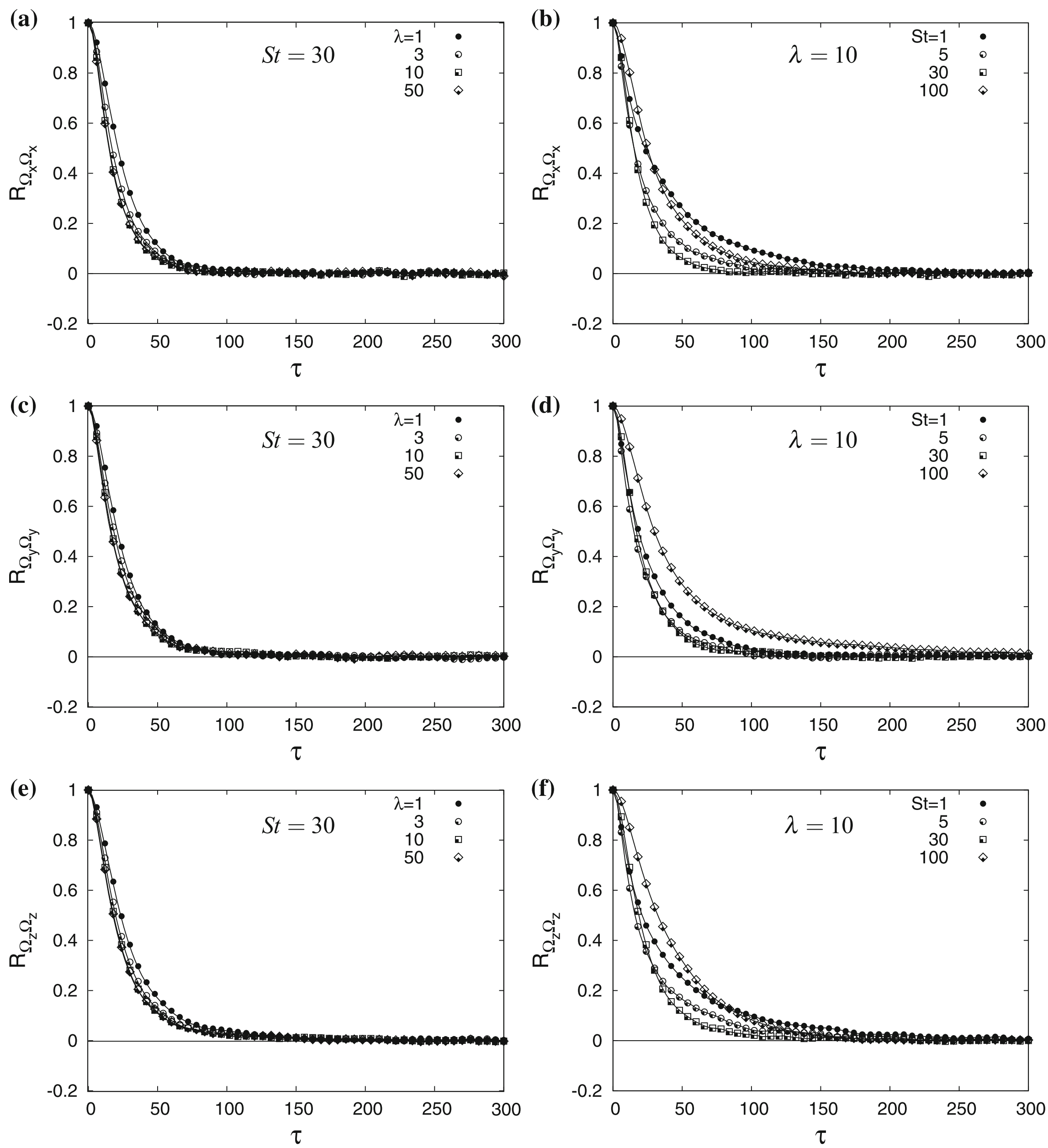

Fig. 7 Lagrangian autocorrelation coefficients of fiber angular velocity, R_{Ω_i,Ω_i}, inside the log layer ($50 < z^+ \leq Re_\tau$). **a**, **b** R_{Ω_x,Ω_x}, **c**, **d** R_{Ω_y,Ω_y}, **e**, **f** R_{Ω_z,Ω_z}. Profiles in **a**, **c** and **e** (resp. **b**, **d**, and **f**) highlight the effect of fiber elongation (resp. inertia) on R_{Ω_i,Ω_i} for the reference case $St = 30$ (resp. $\lambda = 10$)

Therefore, changes of T_L^{ii} are strongly connected to both elongation and inertia, and it is difficult to highlight clear trends, especially at large St (at small St, it appears that timescales are strongly reduced for short fibers and increase again for large fibers). Inertia-induced effects on Lagrangian timescales can also be inferred from Table 1. In the log layer, both T_L^{xx} and T_L^{zz} decrease with inertia up to $St = 30$ and increase again for larger values of the Stokes number, whereas T_L^{yy} reaches the minimum values for $St = 5$. In the buffer layer, the minimum value of the timescales is always that of the $St = 5$ fibers. In the viscous sublayer, there is a general increase in the timescales with fiber inertia, and minima are always found for $St = 1$. A combined evaluation of Table 1 and Figs. 7, 8, 9 provides evidence that correlations for fibers initially located in the log region decrease more slowly than those in the buffer layer, which in turn decrease more slowly than those in the viscous layer. A similar trend was observed for Lagrangian autocorrelations of translational velocity and

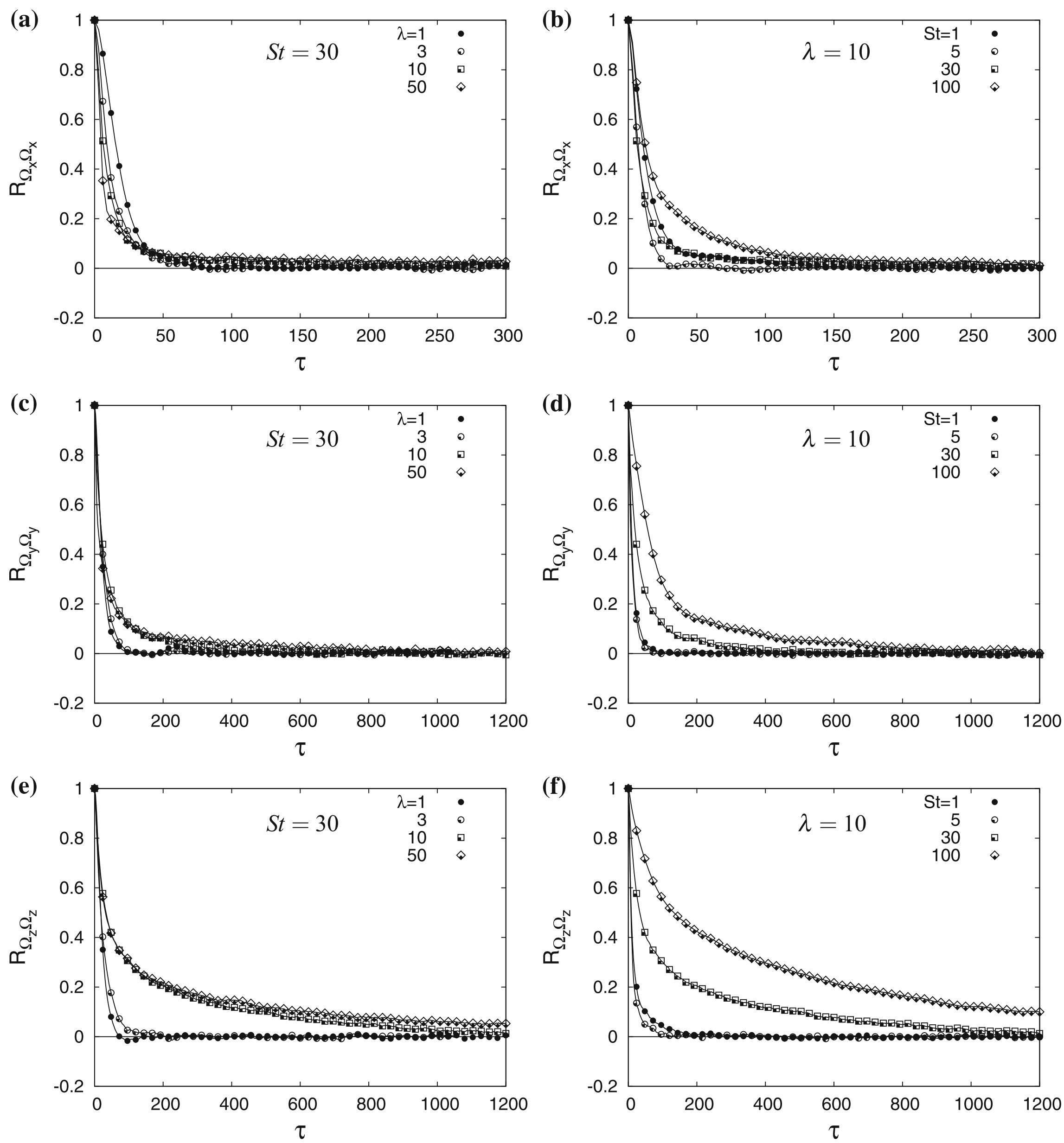

Fig. 8 Lagrangian autocorrelation coefficients of fiber angular velocity, R_{Ω_i,Ω_i}, inside the buffer layer ($5 < z^+ \leq 50$). **a**, **b** R_{Ω_x,Ω_x}, **c**, **d** R_{Ω_y,Ω_y}, **e**, **f** R_{Ω_z,Ω_z}. Profiles in **a**, **c** and **e** (resp. panels **b**, **d** and **f**) highlight the effect of fiber elongation (resp. inertia) on R_{Ω_i,Ω_i} for the reference case $St = 30$ (resp. $\lambda = 10$)

acceleration of spherical particles in turbulent channel flow [20,22] and for Lagrangian autocorrelations of orientation and rotation rate in HIT [6], corroborating further the adequacy of the Lagrangian approach.

3.3 Statistics of rotational turbulent diffusivity

From the autocorrelation coefficients presented in Sect. 3.2, it is possible to calculate the rotational turbulent diffusivity, normalized by the angular velocity variance to allow direct comparison among the different fiber families:

$$\Gamma_\Omega(\tau) = \int_0^\tau R_{\Omega_i,\Omega_i}(t)\mathrm{d}t. \tag{10}$$

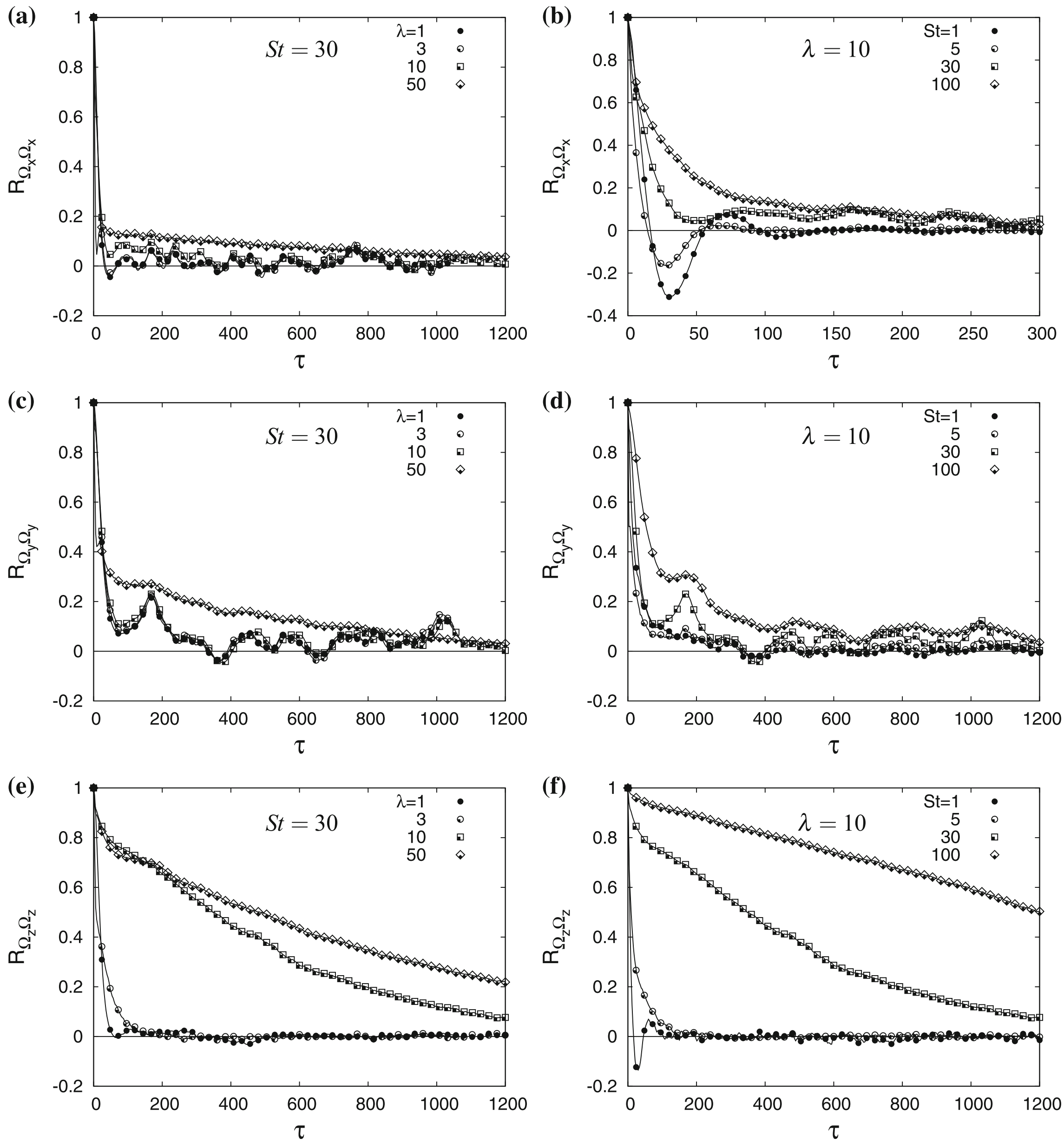

Fig. 9 Lagrangian autocorrelation coefficients of fiber angular velocity, R_{Ω_i,Ω_i}, inside the viscous sublayer ($0 < z^+ \leq 5$). **a**, **b** R_{Ω_x,Ω_x}, **c**, **d** R_{Ω_y,Ω_y}, **e**, **f** R_{Ω_z,Ω_z}. Profiles **a**, **c**, and **e** (resp. panels **b**, **d**, and **f**) highlight the effect of fiber elongation (resp. inertia) on R_{Ω_i,Ω_i} for the reference case $St = 30$ (resp. $\lambda = 10$)

If the time evolution of fiber angular velocity can be described by an OU-like process, then rotational diffusivity is expected to increase exponentially according to the relation:

$$\Gamma_{\Omega_i}(\tau) = T_L^{ii}\left(1 - e^{-\frac{\tau}{T_L^{ii}}}\right). \tag{11}$$

When the exponential term drops to zero for $\tau >> T_L^{ii}$, $\Gamma_{\Omega_i}(\tau)$ tends toward a constant value (known as the Fickian asymptote), which is equal to the Lagrangian integral timescale: $\hat{\Gamma}_{\Omega_i} = T_L^{ii}$.

In Figs. 10, 11, and 12, we compare, for each subregion of the channel, the time evolution of normalized rotational diffusivities computed from our DNS+LPT database with the corresponding prediction given by Eq. (11), with T_L^{ii} calculated as defined in Eq. (9). As anticipated by the discussion of Fig. 10, the agreement

Table 1 Values of the Lagrangian integral timescales for fiber angular velocity, T_L^{ii}, calculated from Eq. (9) over the time window $\Delta\tau = 1{,}200$ considered to compute the Lagrangian autocorrelation coefficients

St	λ	Viscous sublayer			Buffer layer			Log layer		
		$(0 \le z^+ \le 5)$			$(5 < z^+ \le 50)$			$(50 < z^+ \le Re_\tau)$		
		T_L^{xx}	T_L^{yy}	T_L^{zz}	T_L^{xx}	T_L^{yy}	T_L^{zz}	T_L^{xx}	T_L^{yy}	T_L^{zz}
1	1	10.57	35.41	24.17	29.62	16.35	33.49	51.32	33.25	49.12
1	3	3.47	21.69	5.03	15.68	14.39	24.17	43.17	30.21	42.28
1	10	3.81	40.22	8.13	18.39	15.90	21.70	40.54	30.10	41.22
1	50	30.68	47.81	7.48	23.43	16.43	21.54	41.29	30.46	41.12
5	1	12.00	40.75	21.47	16.83	15.40	22.13	32.40	26.30	36.83
5	3	9.86	30.38	5.46	9.13	11.33	17.38	26.64	23.83	31.84
5	10	4.58	33.78	29.77	10.44	13.68	15.56	25.92	24.21	30.54
5	50	26.31	54.02	38.51	15.97	19.17	16.24	25.62	24.47	30.54
30	1	22.55	56.28	26.61	20.09	23.64	22.96	28.32	27.76	34.26
30	3	24.88	58.03	28.30	14.46	26.01	29.93	23.65	25.67	29.70
30	10	34.54	61.82	∼450	17.62	48.82	∼130	21.65	24.73	27.47
30	50	41.66	∼110	∼610	19.03	63.01	∼160	21.34	24.06	27.42
100	1	54.11	85.76	47.14	43.37	43.71	46.58	49.81	54.46	55.01
100	3	72.28	∼140	∼130	31.29	49.62	78.11	40.89	52.16	49.30
100	10	82.26	∼210	∼1,200	32.58	∼120	∼350	36.31	49.09	45.45
100	50	∼440	∼1,200	∼1,850	∼80	∼250	∼460	33.42	45.81	44.49

Values preceded by a tilde (∼) correspond to autocorrelation coefficients that do not decay to zero within $\Delta\tau$ and were thus computed on a wider time window, $\Delta\tilde{\tau} = 1{,}800$

between numerical results and theoretical prediction in the log region is excellent, even at short times. At longer times, the $\Gamma_{\Omega_i}(\tau)$ curves recover the Fickian asymptote, as expected. This confirms that fiber rotation in the central region of the channel can be modeled as an OU process provided that angular velocities have a Gaussian distribution. Examining the left-hand panels of Fig. 10, we note that spherical particles exhibit the highest rotational diffusivity in all flow directions: for a given value of the angular velocity variance, rotational diffusivity for fibers is observed to decrease as fiber elongation increases up to $\lambda = 10$ (further increase of λ does not seem to alter $\Gamma_{\Omega_i}(\tau)$ significantly). Right-hand panels in Fig. 10 highlight the effect of inertia on $\Gamma_{\Omega_i}(\tau)$: in this case, the normalized rotational diffusivity decreases monotonically up to $St = 30$ and then increases for larger values of St. In the spanwise and wall-normal directions, the increase in $\Gamma_{\Omega_i}(\tau)$ is notable and attains values larger than for spherical particles.

In the buffer layer (Fig. 11), Eq. (11) provides a good fit of numerical results only for spherical particles and fibers with either small elongation ($\lambda < 10$) or small inertia ($St << 30$). For long inertial fibers, theoretical predictions generally overestimate the growth of $\Gamma_{\Omega_i}(\tau)$. As expected, deviations become larger in the viscous sublayer (Fig. 12) where theoretical predictions match numerical results only for $\Gamma_{\Omega_z}(\tau)$ of spherical particles and of short fibers with $L^+/\tau_K^+ \sim \mathcal{O}(1)$ and with small inertia. In all other cases, fiber rotation is not exponentially autocorrelated, and it may be concluded that angular velocities have a non-Gaussian distribution due to strong shear, high turbulence anisotropy, and velocity gradients that are not δ-correlated [4].

3.4 PDF of fiber angular velocities

An OU process is characterized by exponentially decaying autocovariance, stationarity, and Gaussian distribution. Based on the discussion of autocorrelation curves, we can conclude that the OU process is not an acceptable model for fiber rotation near the wall. In this subsection, we aim at verifying the applicability of such a model in the center of the channel, where mean shear and flow anisotropy produce much weaker effects on fiber rotation. To do so, we evaluate the PDF of fiber angular velocities, PDF(Ω_i), when the rotation process has reached a statistically stationary state (note that the driving flow is also stationary). In Fig. 13, we show the behavior of PDF(Ω_i) in the different subregions of the channel for the reference case of $St = 30$ fibers with $\lambda = 10$. Since we are particularly interested in the properties of the PDF in the log layer (solid line), we included also the Gaussian PDF (dot-dashed line) that has the same mean value, $\mu = 0$, and standard deviation, σ_{Log}. Results for the other fiber families are qualitatively similar and are

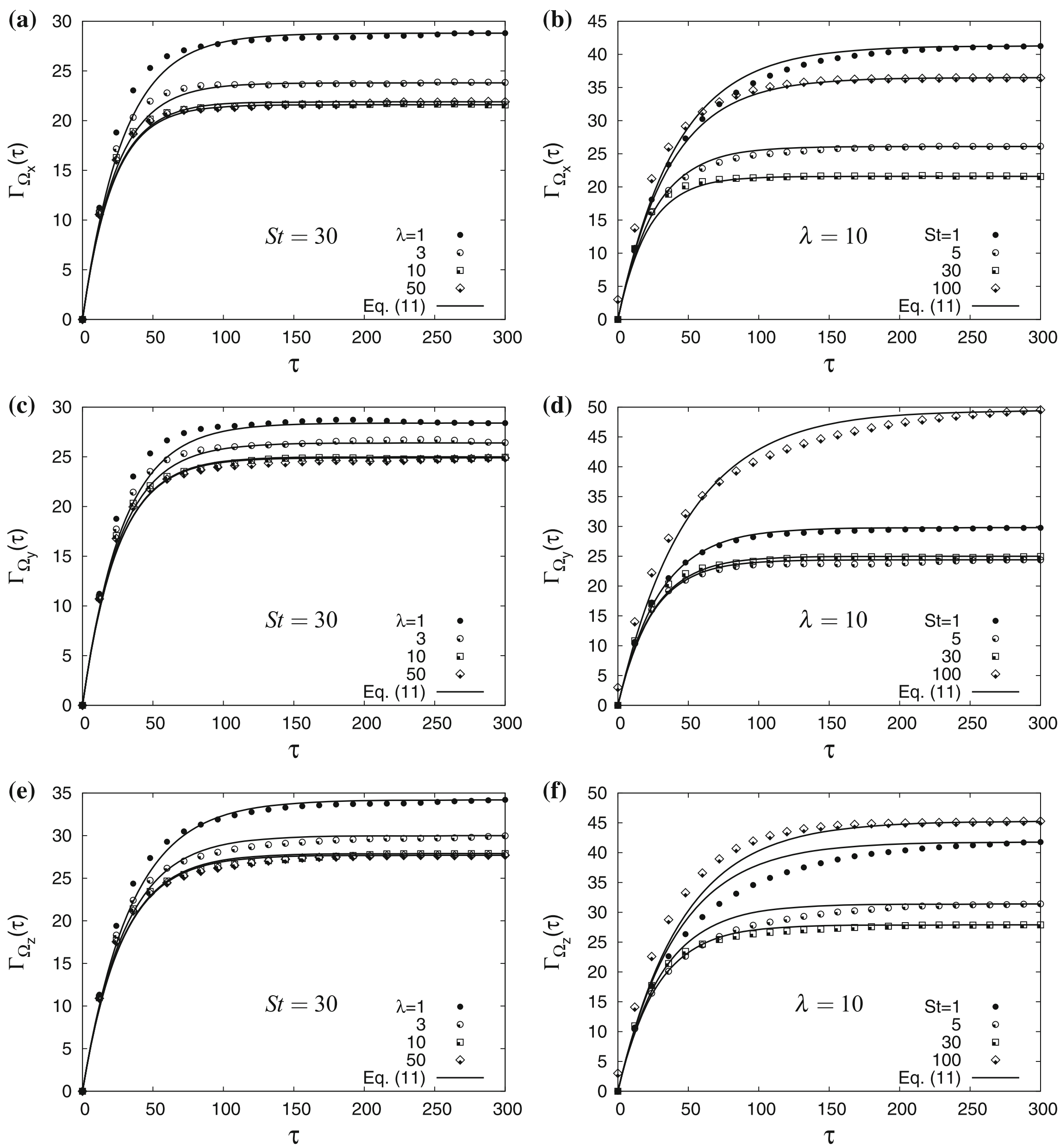

Fig. 10 Rotational turbulent diffusivities, $\Gamma_{\Omega_i}(\tau)$, inside the log layer ($50 < z^+ \le Re_\tau$). **a**, **b** $\Gamma_{\Omega_x}(\tau)$, **c**, **d** $\Gamma_{\Omega_y}(\tau)$, **e**, **f** $\Gamma_{\Omega_z}(\tau)$. Profiles in **a**, **c**, and **e** (resp. **b**, **d**, and **f**) highlight the effect of fiber elongation (resp. inertia) on Γ_{Ω_i} for the reference case $St = 30$ (resp. $\lambda = 10$)

thus omitted for the sake of brevity. Post-processed data files, however, are made available in the public database.

Several observations can be made from Fig. 13. First, the PDF in the log layer is very close to Gaussian for all angular velocity components. Deviations are observed in the tails of the distribution, but only for the values of Ω_i at least two times larger than σ_{Log}. Computed PDFs have longer and higher tails, indicating the presence of rare events with high rotation rates [4]. This result is common to all fiber families considered in this study and, together with the previously observed exponential decay of autocorrelation coefficients, indicates that fiber rotation follows an OU process with the exception of intense events characterized by high fluctuations of Ω_i. It also confirms that rotation in the center of the channel is little affected by mean shear and turbulence anisotropy [23,25,27]. Second, the PDFs of the streamwise and wall-normal angular velocities, which have zero mean value, appear similar in the three subregions of the channel (with deviations from Gaussianity in

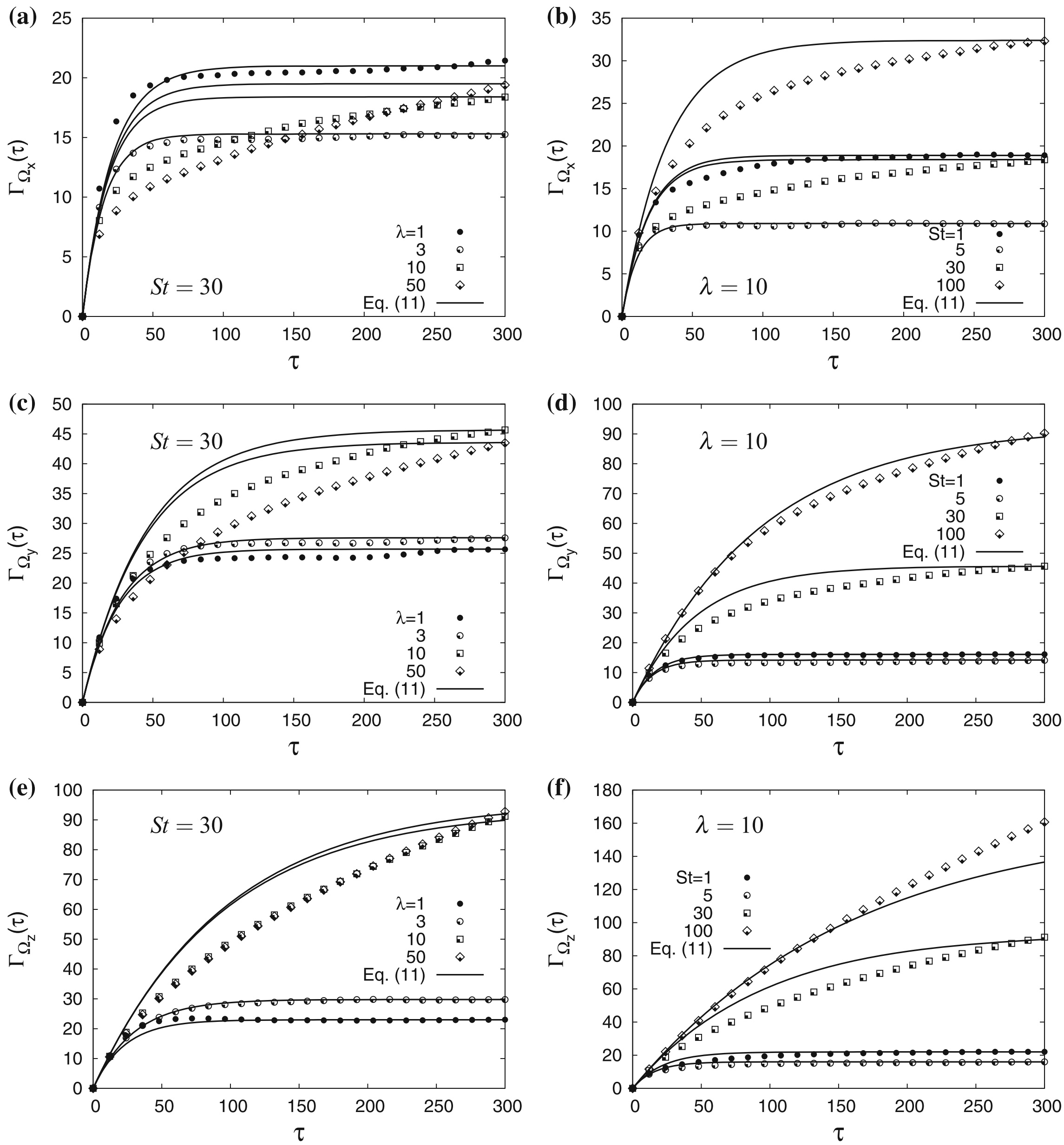

Fig. 11 Rotational turbulent diffusivities, $\Gamma_{\Omega_i}(\tau)$, inside the buffer layer ($5 < z^+ \leq 50$). **a**, **b** $\Gamma_{\Omega_x}(\tau)$, **c**, **d** $\Gamma_{\Omega_y}(\tau)$, **e**, **f** $\Gamma_{\Omega_z}(\tau)$. Profiles in **a**, **c**, and **e** (resp. **b**, **d**, and **f**) highlight the effect of fiber elongation (resp. inertia) on Γ_{Ω_i} for the reference case $St = 30$ (resp. $\lambda = 10$)

the tails of the curve), whereas the distribution of spanwise angular velocity, characterized by nonzero mean value (see Fig. 3), samples a wider range of rotation values. Third, the shape of the PDF is not much dependent on the elongation of the fiber as demonstrated by the insets in each panel of Fig. 13. This is in agreement with previous observations that particle shape has minor effects on rotation statistics [9].

4 Concluding remarks

In this work, we study the dynamics of rigid fibers in wall-bounded turbulence. We perform a parametric Eulerian–Lagrangian study in the $(St,\ \lambda)$ space, to characterize from a statistical point of view fiber rotation. Present DNS-based results, obtained for the reference case of turbulent channel flow, indicate that the process

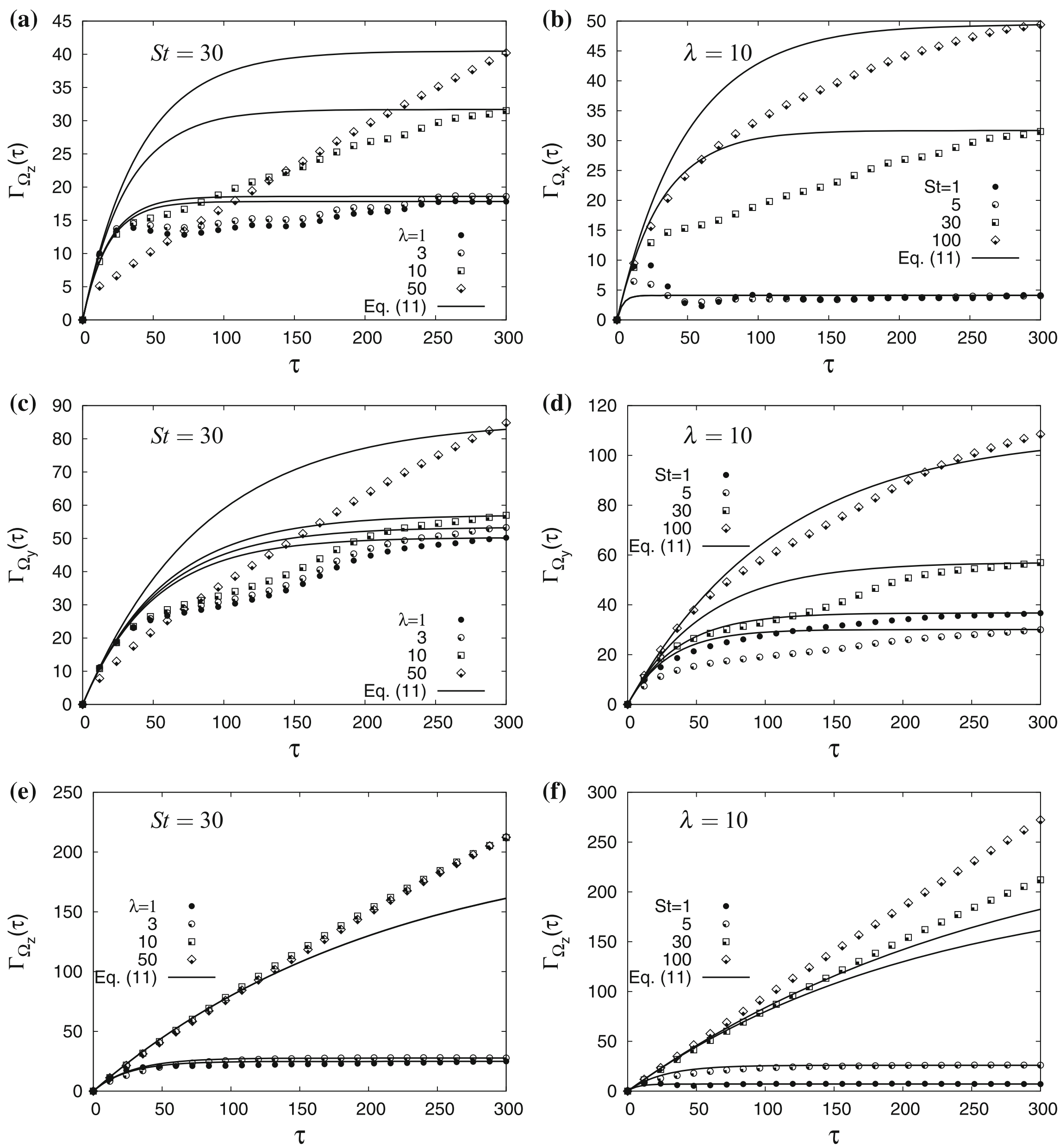

Fig. 12 Rotational turbulent diffusivities, $\Gamma_{\Omega_i}(\tau)$, inside the viscous sublayer ($0 < z^+ \leq 5$). **a**, **b** $\Gamma_{\Omega_x}(\tau)$, **c**, **d** $\Gamma_{\Omega_y}(\tau)$, **e**, **f** $\Gamma_{\Omega_z}(\tau)$. Profiles in **a**, **c**, and **e** (resp. **b**, **d**, and **f**) highlight the effect of fiber elongation (resp. inertia) on Γ_{Ω_i} for the reference case $St = 30$ (resp. $\lambda = 10$)

of rotational diffusion exhibits Gaussian properties in the center of the channel: Theoretical predictions provide a very good approximation of numerical results regardless of particle inertia and shape, which only modify the autocorrelation decay rate and, in turn, the integral fiber timescales. In this region, autocorrelation curves decay exponentially, and no significant deviations of angular velocity distribution from gaussianity are observed: these findings suggest that fiber rotation can be adequately modeled as a Gaussian process, a diffusion process, and an OU process. The hypothesis of nearly homogeneous dispersion thus appears acceptable for fiber rotation, and standard diffusion laws similar to those governing low-order translational statistics such as turbulent diffusion coefficient or mean square displacement distributions can be applied [21]. Rather expected, in the viscous sublayer (up to 5 viscous units from the wall in our simulations), diffusion laws generally fail in the streamwise and spanwise directions, indicating that wall-parallel fiber rotation cannot be modeled with a

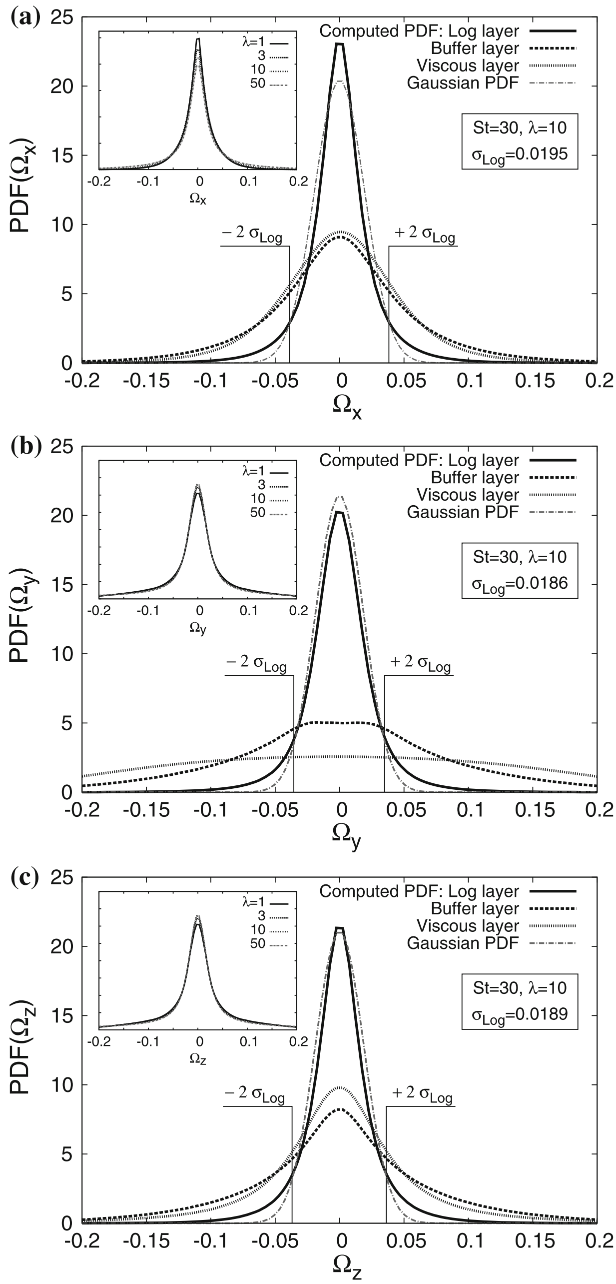

Fig. 13 Probability density function of fiber angular velocity components, PDF(Ω_i), in the different subregions of the channel for the reference case $St = 30$ and $\lambda = 10$. For comparison purposes, the Gaussian PDF with same mean and standard deviation (σ_{Log}) of the PDF computed in the log layer is shown. The inset in each panel highlights the effect of fiber elongation on the PDF (for the reference case of $St = 30$). **a** PDF(Ω_x), **b** PDF(Ω_y), **c** PDF(Ω_z)

standard OU process in regions of strong anisotropy. In the wall-normal direction, however, there is still good agreement between simulations and theory for short fibers with low inertia. Intermediate between these limiting cases is fiber rotation in the buffer layer (corresponding to the region between 5 and 50 viscous units from the wall), which obeys homogeneous diffusion behavior in all directions for small fiber elongation ($\lambda \leq 3$) and relatively small fiber inertia ($St \leq 5$). The statistics for Lagrangian autocorrelation curves of fiber angular velocity and for fiber rotational diffusivity (normalized by the fiber angular velocity variance) examined in the present study assess the adequacy of Lagrangian tracking of point fibers in reproducing the interaction between fiber anisotropy and turbulence anisotropy and the resulting complex behavior. Statistics also emphasize the inaccuracy that may be expected from stochastic models for fiber dispersion, which represent fiber rotation as a statistically stationary Gaussian process. We provide statistics and raw data (https://www.fp1005.cism.it) that can be used as benchmark for validating the performance of dispersion models for fibers in high shear region and/or developing more precise models.

As further development of this study, it would be interesting to analyze fiber rotation with respect to the fiber frame of reference: statistical characterization of the fiber angular velocity relative to corotating axes, a rather complicated task to accomplish experimentally but simple numerically, would provide useful information about changes to motile diffusion and drag, useful when studying the behavior of motile organisms [9].

Acknowledgments Financial support from the Regional Authority of Friuli Venezia Giulia under Grant *"Nuove metodologie per la riduzione e la gestione di emissioni di COV e particolato per l'industria di pannelli di particelle e fibra di legno"* is gratefully acknowledged. COST Action FP1005 is also gratefully acknowledged.

References

1. Lundell, F., Soderberg, L.D., Alfredsson, P.H.: Fluid mechanics of papermaking. J. Fluid Mech. **43**, 195–217 (2011)
2. Jarecki, L., Blonski, S., Blim, A., Zachara, A.: Modeling of pneumatic melt spinning processes. J. Appl. Polym. Sci. **125**, 4402–4415 (2012)
3. Yashiro, S., Sasaki, H., Sakaida, Y.: Particle simulation for predicting fiber motion in injection molding of short-fiber-reinforced composites. Compos. Part A Appl. Sci. Manuf. **43**, 1754–1764 (2012)
4. Parsa, S., Calzavarini, E., Toschi, F., Voth, G.A.: Rotation rate of rods in turbulent fluid flow. Phys. Rev. Lett. **109**, 134501 (2012)
5. Lin, J.Z., Liang, X.Y., Zhang, S.L.: Numerical simulation of fiber orientation distribution in round turbulent jet of fiber suspension. Chem. Eng. Res. Des. **90**, 766–775 (2012)
6. Shin, M., Koch, D.L.: Rotational and translational dispersion of fibers in isotropic turbulent flows. J. Fluid Mech. **540**, 143–173 (2005)
7. Moosaie, A., Le Duc, A., Manhart, M.: A priori analysis of a closure model using the reconstruction of the orientation distribution function in flow of fiber suspensions. Comput. Mech. **48**, 451–459 (2011)
8. Olson, J.A., Kerekes, R.J.: The motion of fibers in turbulent flow. J. Fluid Mech. **377**, 47–64 (1998)
9. Meyer, C.R., Variano, E.: Rotational diffusion of particles in turbulence. arXiv:1301.0150, 2012.
10. Bezuglyy, V., Mehlig, B., Wilkinson, M., Nakamura, K., Arvedson, E.: Generalized Ornstein–Uhlenbeck processes. J. Math. Phys. **47**, 073301 (2010)
11. Reynolds, A.M.: Lagrangian stochastic modeling of anomalous diffusion in two-dimensional turbulence. Phys. Fluids **14**, 1442–1451 (2002)
12. Taylor, G.I.: Diffusion by continuous movements. Proc. Lond. Math. Soc. **20**, 196 (1921)
13. Yeung, P.K., Pope, S.B.: Lagrangian statistics from direct numerical simulations of isotropic turbulence. J. Fluid Mech. **207**, 531 (1989)
14. Mordant, N., Metz, P., Michel, O., Pinton, J.-F.: Measurement of Lagrangian velocity in fully developed turbulence. Phys. Rev. Lett. **87**, 214501 (2001)
15. Sato, Y., Yamamoto, K.: Lagrangian measurements of fluid-particle motion in an isotropic turbulent field. J. Fluid Mech. **175**, 183 (1987)
16. Voth, G.A., La Porta, A., Crawford, A.M., Alexander, J., Bodenschatz, E.: Measurement of particle acceleration in fully developed turbulence. J. Fluid Mech. **469**, 121 (2002)
17. Snyder, W.H., Lumley, J.L.: Some measurements of particle velocity autocorrelation functions in a turbulent flow. J. Fluid Mech. **48**, 41–47 (1971)
18. Weiss, J.B., Provenzale, A., McWilliams, J.C.: Lagrangian dynamics in high-dimensional point-vortex systems. Phys. Fluids **10**, 1929–1942 (1998)
19. Yeung, P.K.: Lagrangian investigations of turbulence. Ann. Rev. Fluid Mech. **34**, 115–142 (2002)
20. Choi, J., Yeo, K., Lee, C.: Lagrangian statistics in turbulent channel flow. Phys. Fluids **16**, 779–793 (2004)
21. Soldati, A., Casal, M., Andreussi, P., Banerjee, S.: Lagrangian simulation of turbulent particle dispersion in electrostatic precipitators. AIChE J. **43**, 1403–1413 (1997)
22. Wang, Q., Squires, K.D., Wu, X.: Lagrangian statistics in turbulent channel flow. Atmosph. Environ. **29**, 2417–2427 (1995)
23. Mortensen, P.H., Andersson, H.I., Gillissen, J.J.J., Boersma, B.J.: Dynamics of prolate ellipsoidal particles in a turbulent channel flow. Phys. Fluids **20**, 093302 (2008)
24. Jeffery, G.B.: The motion of ellipsoidal particles immersed in a viscous fluid. Proc. R. Soc. **102**, 161–179 (1922)
25. Marchioli, C., Fantoni, M., Soldati, A.: Orientation, distribution and deposition of elongated, inertial fibers in turbulent channel flow. Phys. Fluids **22**, 033301 (2010)
26. Soldati, A., Marchioli, C.: Physics and modelling of turbulent particle deposition and entrainment: review of a systematic study. Int. J. Multiph. Flow **35**, 827–839 (2009)
27. Zhang, H., Ahmadi, G., Fan, F.G., McLaughlin, J.B.: Ellipsoidal particles transport and deposition in turbulent channel flows. Int. J. Multiph. Flow **27**, 971–1009 (2001)
28. Gallily, I., Cohen, A.: On the orderly nature of the motion of nonspherical aerosol particles. J. Colloid Interface Sci. **68**, 338–356 (1978)
29. Brenner, H.: The Stokes resistance of an arbitrary particle. Chem. Eng. Sci. **18**, 1–25 (1963)

30. Fan, F.G., Ahmadi, G.: A sublayer model for wall deposition of ellipsoidal particles in turbulent streams. J. Aerosol Sci. **25**, 831–840 (1995)
31. Shapiro, M., Goldenberg, M.: Deposition of glass fiber particles from turbulent air flow in a pipe. J. Aerosol Sci. **24**, 65–87 (1993)